Solar-Terrestrial Physics. 2026, vol. 12, iss. 2, pp. 34–42. DOI: 10.12737/stp-122202604. © 2026 B. Tsegmed, B. Namuun. Published by INFRA-M Academic Publishing House

DOI: 10.12737/stp-122202604
EDN: ZESDHZ

Received August 26,.2025
Accepted December 15, 2025

STATISTICAL STUDY OF PREDICTIVE PARAMETERS FOR GEOMAGNETIC STORMS DURING SOLAR CYCLES 23–24

B. Tsegmed
Institute of Astronomy and Geophysics MAS, Ulaanbaatar, Mongolia, tseg@iag.ac.mn

B. Namuun
Institute of Astronomy and Geophysics MAS, Ulaanbaatar, Mongolia, namuun@iag.ac.mn

Abstract. This work focuses on exploring the correlation between solar activity parameters and geomagnetic activity during solar cycles 23 and 24. The analysis includes variables such as solar wind speed V_{SW}, proton density N_p, solar wind dynamic pressure P_{SW}, and interplanetary magnetic field components B_z and B_y, along with energy-related parameters E_{SW}, $d\varphi/dt$, ε. Correlation coefficients and time lags were calculated between these solar wind, magnetic field, and energy parameters and geomagnetic indices *SYM-H*, *AE* for storms driven by CME and CIR. The analysis of time delays Δt of auroral activity relative to the energy parameters and the interplanetary magnetic field component B_z for storms of both types has revealed durations ranging from 30 to 60 min, whereas for the ring current the delays ranged from 6 to 24 hrs.

Keywords: correlation coefficient, solar wind parameters, interplanetary magnetic field parameter, coronal mass ejection, corotating interaction region, geomagnetic activity parameters.

INTRODUCTION

Among the dangerous natural phenomena are geomagnetic storms and substorms. These phenomena can disrupt the operation of power grids, communication lines, as well as electrical equipment in aircraft and spacecraft. Their primary sources are active processes on the Sun, such as solar flares and coronal holes.

During solar flares, plasma and magnetic fields are ejected from the Sun's corona, known as coronal mass ejection (CME). Other sources include long-lasting coronal holes, which produce persistent high-speed streams of solar wind. When these streams interact with slower solar wind ones, compression zones form, known as corotating interaction regions (CIRs). These streams propagate through the interplanetary medium, forming the solar wind that reaches Earth. The collision of the solar wind with our planet's magnetic field leads to the occurrence of geomagnetic storms and substorms.

The energy, momentum, and mass of the solar wind are transferred into the magnetosphere primarily through magnetic reconnection processes in the dayside magnetosphere [Paschmann et al., 1979]. However, there are other ways in which solar wind energy, momentum, and mass can penetrate the magnetosphere, for example, directly through the cusps [Kremser, Lundin, 1990], impulsive plasma penetration across the magnetopause [Gunell et al., 2012], diffusion at the magnetospheric boundary [Tsurutani, Thorne, 1982], and during periods of northward orientation of the interplanetary magnetic field (IMF), through the Kelvin-Helmholtz instability [Hasegawa et al., 2004] and high-latitude reconnection [Fuselier et al., 2000]. Magnetic reconnection is particularly effective under southward IMF conditions [Yamada et al., 2010]. The primary convection in the magnetosphere is expected to be controlled by dayside magnetospheric reconnection combined with reconnection at the distant neutral line in the magnetotail — the so-called Dungey cycle [Dungey, 1961].

Potapov [2013] has examined the influence of ultra-low frequency (ULF) wave activity in high-speed solar wind streams on Earth's magnetosphere, with an emphasis on the differences between CME and CIR. It is specifically the ULF waves that affect the geomagnetic field, producing geomagnetic pulsations, which are oscillations of the geomagnetic field. These effects depend on the type of high-speed solar wind stream (HSS) interacting with the magnetosphere. CIRs generate wave-like ULF activity that gradually increases before the stream front and reaches a maximum a few hours after its passage. This activity then gradually decays over the course of several days. CME, on the other hand, produces sharp, irregular ULF activity that peaks at the stream front and quickly diminishes within ~20 hrs [Potapov, 2013].

Research on the relationship between solar wind (SW) parameters, IMF, and geomagnetic field indices has been conducted for decades. Predicting geoeffective geomagnetic storms to mitigate potential risks has become a crucial aspect of space weather studies. To date, numerous scientific studies have been carried out to develop solutions for preventing such phenomena, analyzing the manifestations and origins of geomagnetic storms, their characteristic features, dependence on solar and interplanetary events, as well as exploring various forecasting methods.

Most forecasting methods involve the use of geomagnetic indices such as *Dst*, *AE*, *PC*, and K_p, which quantify the intensity and strength of geomagnetic storms, as the most extreme events pose the greatest potential threat to technological systems. Geomagnetic activity is primarily driven by the interaction between the solar wind and Earth's magnetosphere, with solar

wind parameters and IMF conditions often serving as key drivers of this activity.

Burton et al. [1975] introduced an algorithm for predicting *Dst* based on solar wind speed, density, and the IMF north-south component. Their results showed strong agreement with ground-based magnetometer measurements of *Dst*.

CME and CIR are recognized as significant drivers of geomagnetic activity because they induce strong disturbances in the geomagnetic field [Hutchinson et al., 2011; Perreault, Akasofu, 1978]. These disturbances lead to the accumulation of substantial energy in the magnetotail and inner magnetosphere, contributing to the intensification of the ring current. Additionally, they influence magnetic activity in the auroral region.

A defining characteristic of a magnetic storm is the decrease in the horizontal component of the magnetic field, described by *Dst*. This decrease results from the ring current encircling Earth [Kamide et al., 1998]. The primary source of the ring current is the plasma sheet, which can be supplied by both solar wind plasma and ionospheric sources [Chen, 2020].

Depending on the region of the magnetosphere where a disturbance and currents occur, intense geomagnetic disturbances can be broadly classified as either geomagnetic storms or substorms [Gonzalez et al., 1994; Kamide et al., 1998]. Observing these phenomena involves measuring geomagnetic disturbances caused by the intensification of associated current systems, namely the auroral electrojet and the ring current. The geomagnetic indices *AE* and *SYM-H* were developed to quantify auroral zone activity and ring current variations, respectively.

Based on the Dungey model, it has been widely recognized that the solar wind speed and the IMF southward components are the primary factors driving the reconnection mechanism [Borovsky, Denton, 2006; Burton et al., 1975; Perreault, Akasofu, 1978]. This mechanism allows plasma flows to penetrate Earth's magnetosphere, transferring energy. Therefore, the combination of the solar wind speed (V) and the IMF B_z component — known as the "energy coupling function" — is commonly used to indirectly estimate the energy transferred from the solar wind.

In previous work [Namuun et al., 2023], we have examined the average correlation between solar wind parameters, IMF parameters, and geomagnetic indices, as well as energy parameters during solar cycles 23–24, using 131 CME-driven and 161 CIR-driven storms. Using this data, we aimed to evaluate prediction parameters and determine possible lead times for hazard warnings.

1. DATA

We utilized data from the OMNI database, which is available at [https://omniweb.gsfc.nasa.gov] and widely acknowledged as the primary source of space weather data for researchers in the field. The foundation of our investigation is high-resolution interplanetary and magnetospheric data with 1-min resolution, which is a composite of measurements taken aboard the ACE, WIND, and IMP-8 spacecraft. For studying the solar terrestrial coupling system, we examined geomagnetic indices, namely *AE* and *SYM-H*, and solar wind parameters such as solar wind speed V_{SW}, proton density N_p, SW dynamic pressure P_{SW}, interplanetary total magnetic field B, and its B_y and B_z components respectively.

One of the widely used indicators of magnetic disturbance intensity is the *Dst* index. It represents the hourly averaged deviation of the horizontal component of Earth's magnetic field. It is calculated using data from four low-latitude ground stations located near the equatorial region, namely Hermanus, Honolulu, Kakioka, and San Juan [Sugiura, 1963] which are located evenly in longitude at a considerable distance from auroral and equatorial electrojets. This index reflects quantitative measure of the intensity of globally symmetrical equatorial electrojet (the "ring current") at the dipole equator on the Earth surface during geomagnetic storms [Lethy et al., 2018; Davis, Sugiura, 1966; Burton et al., 1975]. A more accurate variant of *Dst*, known as the *SYM-H* index, has recently become widely used in space weather research due to its high time resolution.

The detailed structure of magnetic field fluctuations associated with currents in the auroral zone (auroral electrojet) is characterized by the auroral electrojet, denoted by *AE*. The geomagnetic index *AE*, as proposed by Davis [Davis, Sugiura, 1966], is one of the indices employed to assess the activity of Earth's magnetosphere and its impact on the environment, including geomagnetic storms and solar flares. Currently, *AE* is calculated from data obtained at 12 observatories located in the Northern Hemisphere at different longitudes between 60° and 70° geomagnetic latitude [Baumjohann, Treumann, 2012]. To numerically describe substorm activity, geomagnetic indices are also used such as *AL* (auroral low), which corresponds to the maximum negative deviation of the *H* component of the magnetic field from the average quiet level at stations of the auroral zone, and *AU* (auroral upper), which is the largest positive variation of the magnetic field. In general, *AE* indicates the substorm intensity by quantifying the enhancement of ionospheric currents in the polar region, which flow along the auroral oval boundary (eastward and westward electrojets).

2. ENERGY COUPLING FUNCTIONS

The combined solar wind parameters represent the energy relationship between the solar wind and Earth's magnetosphere. The energy coupling functions of the solar wind and magnetosphere are calculated through the following empirical formulas. The pondermotive force named Akasofu function correlates not only with magnetic storms but also with individual substorms [Akasofu, 1981]. It is expressed as [Perreault, Akasofu, 1978]:

$$\varepsilon = V_{SW} B^2 \sin^4(\theta/2) l_0^2.$$

Where l_0 is a constant length (~$7R_E$, $R_E = 6371$ km is the Earth radius). The scaling factor l_0 was obtained by considering the magnetospheric disturbance phenomena as a manifestation of the dissipation process of energy produced by the solar wind—magnetosphere coupling; θ is the projection of the IMF polar angle onto the YZ plane in solar magnetospheric coordinates, and

$$\theta = \tan^{-1}\left(\left|B_y\right|/\left|B_z\right|\right),\ B_z > 0,$$

$$\theta = 180^\circ - \tan^{-1}\left(\left|B_y\right|/\left|B_z\right|\right),\ B_z < 0.$$

The Akasofu function depends not only on IMF clock angle on the YZ plane, but also on $V_{SW}B^2$. $V_{SW}B$ represents the solar wind electric field that plays an essential role in the magnetospheric convection [Burton et al., 1975].

Moreover, E_{KL} and $d\varphi/dt$ also depend on the solar wind electric field and IMF clock angle. E_{KL}, the mean electric field at the magnetopause, is expressed as [Kan, Lee, 1979]

$$E_{KL} = V_{SW}B\sin^2(\theta/2).$$

The magnetic flux $d\varphi/dt$ represented by [Newell et al., 2007],

$$\frac{d\varphi}{dt} = V_{SW}^{4/3}B^{2/3}\sin^{8/3}(\theta/2)$$

is proportional to the rate at which the magnetic flux is opened at the magnetopause, whereas the open magnetic flux depends on E_{KL}. Thus, E_{KL} and $d\varphi/dt$ correlate with the dayside magnetic reconnection that transports the solar wind mass, energy, and IMF into the magnetosphere.

3. METHODOLOGY

To determine causal relationships and their time lag, we have employed a method for assessing delayed dependence between SW data, IMF data, and geomagnetic indices.

In the case of two continuously varying infinite-duration signals $x(t)$ and $y(t)$, the cross-correlation function c_{xy} at time lag τ is defined by the integral expression:

$$c_{xy}(\tau) = \int_{-\infty}^{\infty} x(t)\, y(t \pm \tau)\, dt.$$

If $y(t) = x(t)$, the function is called autocorrelation.

For the classical case of stationary and ergodic time series $x(i)$, $y(i)$, where $i = 1 - n$ (typical in physical and technical applications), this expression is refined as follows:

$$c_{xy}(\tau) = \frac{1}{n-\tau}\frac{\sum_{i=1}^{n-\tau}\left(x(i) - M_x\right)\left(y(i+\tau) - M_y\right)}{S_x S_y}$$

where M_x, M_y are the mean values, S_x, S_y are the standard deviations.

To determine the correlation between solar wind parameters, the interplanetary magnetic field and geomagnetic activity indices, the average behavior of the selected parameters is calculated using the superposed epoch analysis (SEA) relative to the minimum *SYM-H* across all selected storm events.

4. RESULTS AND DISCUSSION

Earth's magnetosphere responds to changes in the solar wind and IMF on different timescales depending on the nature of the interaction. Some processes may occur rapidly (e. g., minutes to hours), while others may be longer (e. g., hours to days).

Therefore, solar wind and IMF parameters are considered as driving parameters since the solar wind is the main driving factor triggering a geomagnetic storm. Thus, reference time series data on geomagnetic indices relative to these SW, IMF parameters, and solar magnetosphere coupling functions is shifted and cross correlation is computed at different time lags.

The cross-correlation analysis of solar wind velocity V_{SW}, IMF B_z and B_y components, proton density N_p, flow pressure P_{SW}, and geomagnetic indices was conducted on selected geomagnetic storms driven by CME and CIR. In addition, we examined the relationship with energy coupling functions.

4.1. Cross-correlation analysis for a CME driven storm

Variation of the cross correlation calculated between *SYM-H* and solar wind, IMF parameters during CME-driven storms at different time lags is shown in Figure 1. The vertical axis represents the correlation coefficient, whereas the horizontal axis corresponds to the time lag in scale of days. Figure 1 depicts that the solar wind velocity, proton density, and dynamic pressure are highly correlated with *SYM-H*, whereas the IMF B_z and B_y components have a moderate correlation, demonstrating bipolar behavior.

4.1.1. CC with SYM-H

At the average time lag Δt=216 min (3^h36^m), the highest correlation coefficient (CC=–0.86) exhibits the solar wind velocity, implying that solar wind velocity variations precede a decrease in *SYM-H* by ~3 hrs and 36 min.

The maximum correlation for P_{SW} (CC=–0.86 at $\Delta t = 08^h30^m$) precedes the maximum correlation for velocity by ~5 hrs, whereas its peak delays the maximum correlation for density by ~8 hrs. This is consistent with the findings of Liang et al. [2015], who observed that a gradual increase in the solar wind pressure began to influence the magnetosphere ~8 hrs before the beginning of the storm main phase. The elevation in the dynamic pressure predominantly results from the increased solar wind density [Liang et al., 2015]. This is not surprising, considering that a significant enhancement in the solar wind dynamic pressure, caused by high-speed energetic plasma traveling through the interplanetary space, impacts Earth's magnetosphere, perturbing the geomagnetic field and contributing to the formation of the ring current [Troshichev, Sormakov, 2019].

The solar wind proton density and velocity are considered to be components of the dynamic pressure, as expressed in the formula $P_{SW} = N_p\left(V_{SW}\right)^2$. It is logical that these three parameters exhibit high correlations with magnetic activity indices, and the time response of *SYM-H*/*AE* to these parameters does not show a big gap in temporal distinctions. A similar result was also represented by Maggiolo et al. [2017], where V_{SW} with *SYM-H* lagged by 26^h was obtained, with *AE* delayed for ~9 hrs indicating an indirect link between the SW and magnetic indices.

Considering the parameter exhibiting the highest correlation in time among the parameters, the density reaches its peak foremost at a time lag Δt~950 min (15^h50^m), CC=–0.71. The IMF B_z correlation is maximum

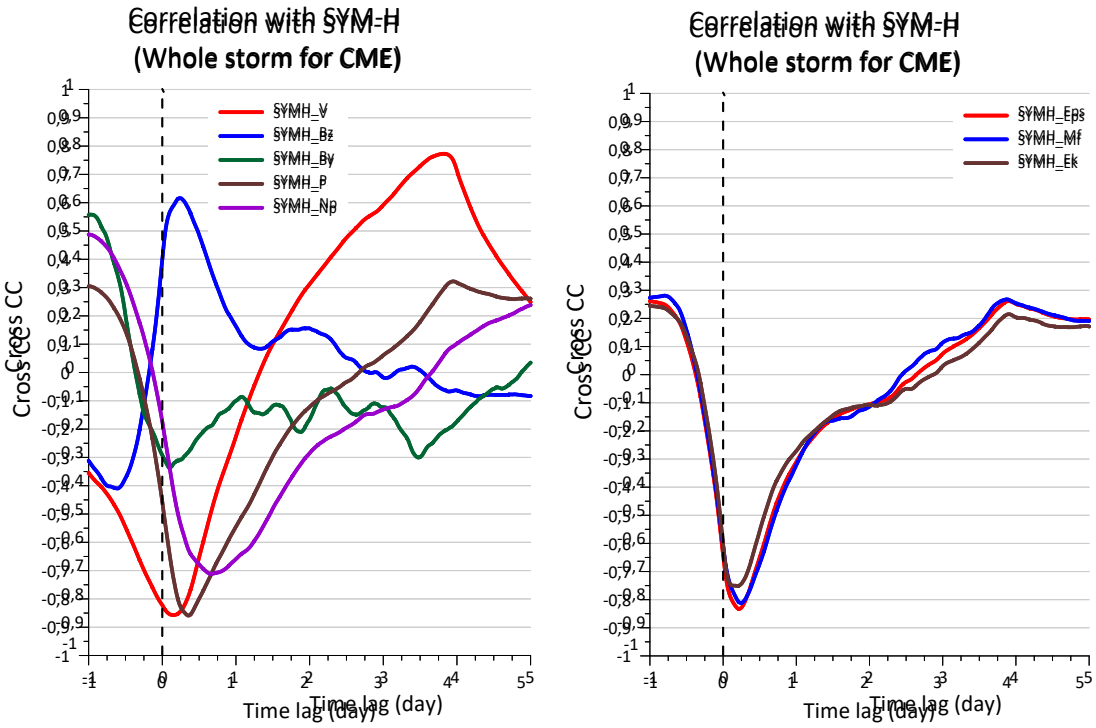

Figure 1. Variation of cross correlation coefficients between *SYM-H* and SW parameters including solar wind speed V_{SW}, SW pressure P_{SW}, proton density N_p, *y*- and *z*-components of the interplanetary magnetic field B_y, B_z respectively (left) and energy coupling functions (right) for CME-driven storm

at ~350 min (5^h50^m) time lag with CC = 0.62. This implies that the influence of IMF B_z can be moderate since according to some studies a decrease in *Dst* might be caused not only by IMF B_z, but also by different processes [Ondoh, 2000].

The IMF B_y component maximum correlation (CC = –0.34) occurs at ~2^h12^m.

The magnetic flux $d\varphi/dt$ maximizes at Δt~350 min (5^h50^m) with a correlation of –0.81, providing the highest value among coupling parameters (Figure 1, right). Secondly, at Δt~290 min (04^h50^m), CC = –0.75 is produced by the E_{KL} function with a time delay of ~60 min compared to the $d\phi/dt$ function. Interestingly, the ε parameter shows its highest correlation at Δt~318 min (05^h18^m), providing CC = –0.83. This implies that the *SYM-H* response is delayed for ~5 hrs relative to the epsilon parameter.

4.1.2. CC with AE

As can be seen from Figure 2 (left), the correlation of the IMF B_z component with *AE* at a time lag of 33 min CC = –0.81. This finding aligns with the work by Polozov [2020], who reported that the influence of IMF B_z on *AE* falls within 1–4 hrs 20–35 min after B_z activation is measured at the L1 point and significant changes are observed in *AE* [Maggiolo et al., 2017; Polozov, 2020; Tsurutani et al., 1990; De Souza et al., 2018). It is widely accepted that magnetic reconnection through which magnetic activity can be initiated is often triggered by southward interplanetary magnetic fields [Dungey, 1961; Tsurutani et al., 1990; Arnoldy, 1971; Meng et al., 1973]. The strong coupling between *AE* activity and IMF B_z was established in [Ondoh, 2000; Rostoker, Fälthammar, 1967]. Additionally, the proton density and dynamic pressure exhibit a significantly high correlation at Δt~317 min, namely, the 5 hrs time delay with CC = 0.85 and at Δt = 180 min (3^h) with CC = 0.95 respectively. The response time of *AE* to the solar wind dynamic pressure is ~5^h, whereas the response to the density takes a little longer time, 4 hrs. Solar wind dynamic pressure activation depends on the solar wind density and velocity [Maggiolo et al., 2017]. Pressure reaches its peak in nearly a few hours (~2 hrs) after the density peaks, which aligns with findings of Maggiolo et al. [2017]. The solar wind velocity at zero-time lag shows a high correlation CC = 0.62, but the highest peak coefficient (CC = –0.69) is observed before *AE* activation at Δt~–325 min (–5^h25^m).

Although there is a relationship at a point, the highest correlation between the indices does not imply a direct impact of *AE* on the velocity, which contradicts the causality principle [Maggiolo et al., 2017] suggesting that there is no direct effect of the parameters. These parameters are in fact related to solar wind specific structure locating in front of CME and CIR, which constitutes a compression region. All this is based on the correlation of B_{SW}/P_{SW} with PC and *AE* indices. No significant correlation is found with the IMF B_y component [Maggiolo et al., 2017].

Figure 2 (right) illustrates cross-correlation variations of energy coupling functions with *AE* for CME. The highest correlation among these energy functions shows the Newell function $d\phi/dt$ peaking at Δt~27min, producing CC = 0.94. Afterwards, the E_{KL} function exhibits a closer relationship with *AE* (Δt~15 min, CC = 0.88). This is consistent with the study by Newell et al. [2007]

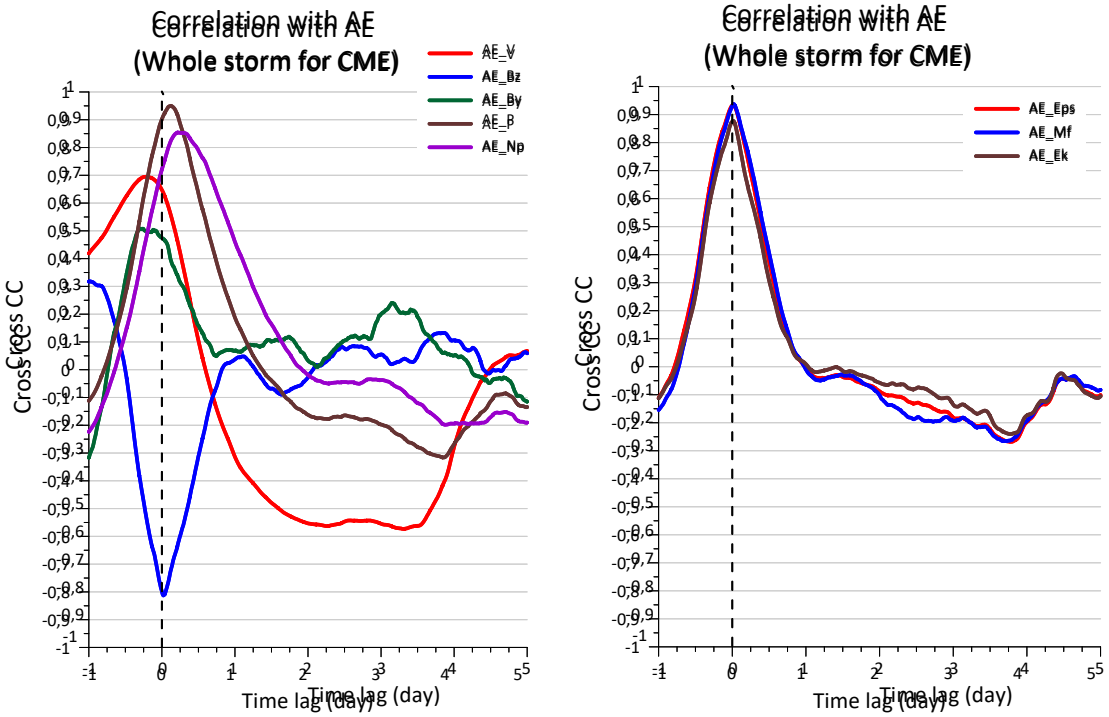

Figure 2. Variation of cross-correlation coefficients between *AE* and SW parameters including the solar wind velocity V_{SW}, pressure P_{SW}, proton density N_p, the interplanetary magnetic field components B_y, B_z respectively (left), and energy coupling functions (right) for a CME-driven storm

that determined which of the 20 candidates of solar wind-magnetosphere functions, widely used in space physics, represents the best correlation with the magnetic activity indices, comprising a total of 10 indices. The authors have found that the best result was obtained with the $d\phi/dt$ function, which represents the rate at which the magnetic flux is opened at the magnetopause [Newell et al., 2007], correlating with 9 out of 10 magnetic indices. The second highly correlated function was the reconnection electric field function composed by Kan and Lee [Kan, Lee, 1979; Kan et al., 1980], denoted by E_{KL}. The E_{KL} parameter is primarily influenced by southward IMF B_z [Stepanov et al., 2021; Tsyganenko, Mukai, 2003].

The efficiency of total energy transfer from the solar wind to the magnetosphere depends on the rate of reconnection at the magnetosphere edges, particularly when IMF B_z shifts southward. Optimal energy transfer occurs when IMF B_z is southward [Dungey, 1961; Tsurutani et al., 2006; De Souza et al., 2018; Rostoker, Fälthammar, 1967; Rout et al., 2023]. According to the widely accepted fact mentioned above, the time lag of the E_{KL} coupling function (Δt=15 m) closely aligns with the time lag between *AE* and B_z (Δt=33 m, CC=–0.81). This suggests a strong dependence of the E_{KL} coupling function on IMF B_z, as the E_{KL} function represents the rate of dayside magnetic reconnection.

4.2. Cross-correlation analysis for a CIR-driven storm

Figure 3 illustrates the cross correlation between SW, IMF parameters and energetic functions, and *SYM-H* during CIR.

The main trend shows that B_z is the first, over a period Δt=4 hrs 30 min (CC=0.71), to trigger the development of the ring current, which corresponds to *SYM-H*. Meanwhile, the solar wind parameters gradually contribute to the enhancement of *SYM-H*. Interestingly, the B_y component exhibits a correlation CC=0.55 prior to the onset of the ring current development (Δt~12 hrs). A similar trend is observed for the solar wind velocity, which has CC=–0.86 with Δt~8 hrs.

As for other solar wind parameters, the dynamic pressure demonstrates a peak correlation CC=–0.85 at Δt~930 min (15^h30^m), whereas the proton density reaches its peak negative correlation CC=–0.67 at Δt~1485 min ($1^d00^h45^m$).

In the case of energy factors, the influence on the ring current begins with the magnetopause current E_{KL} at Δt ~4^h48^m and a correlation coefficient (CC) of –0.75. Then, the magnetic flux $d\phi/dt$ correlates at Δt~5^h34^m with CC=–0.92; and the ponderomotive force ε, at Δt ~6^h00^m with CC=–0.83 (Figure 3, right).

AE correlates (Figure 4, right) with B_z, N_p, and P_{SW} for a coefficient value of –0.82, 0.76, and 0.90 at time lag of 1^h00^m, 18^h28^m, and 06^h20^m respectively. Although *AE* shows a significant relationship with V_{SW}, the peak correlation (CC=0.83) of the solar wind velocity V_{SW} is delayed for 18 hrs 35 min relative to *AE*. This delay is attributed to the distinct velocity profile observed during CIR. It has been known that the velocity progressively increases, in particular in intensity, whereas other solar wind parameters begin to decrease especially during the recovery phase [Richardson, Cane, 1996].

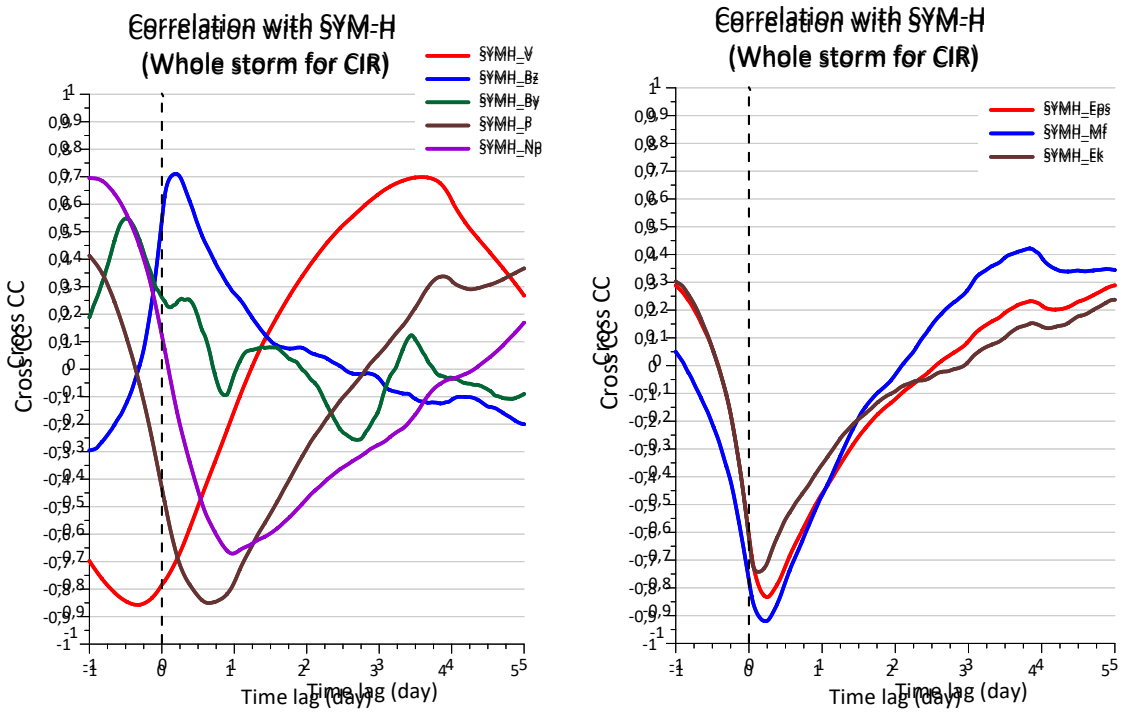

. Variation of cross correlation coefficients between *SYM-H* and SW parameters including solar wind speed V_{SW}, SW pressure P_{SW}, proton density N_p, *y*- and *z*-components of the interplanetary magnetic field B_y, B_z respectively (left) and energy coupling functions (right) for for CIR-driven storm

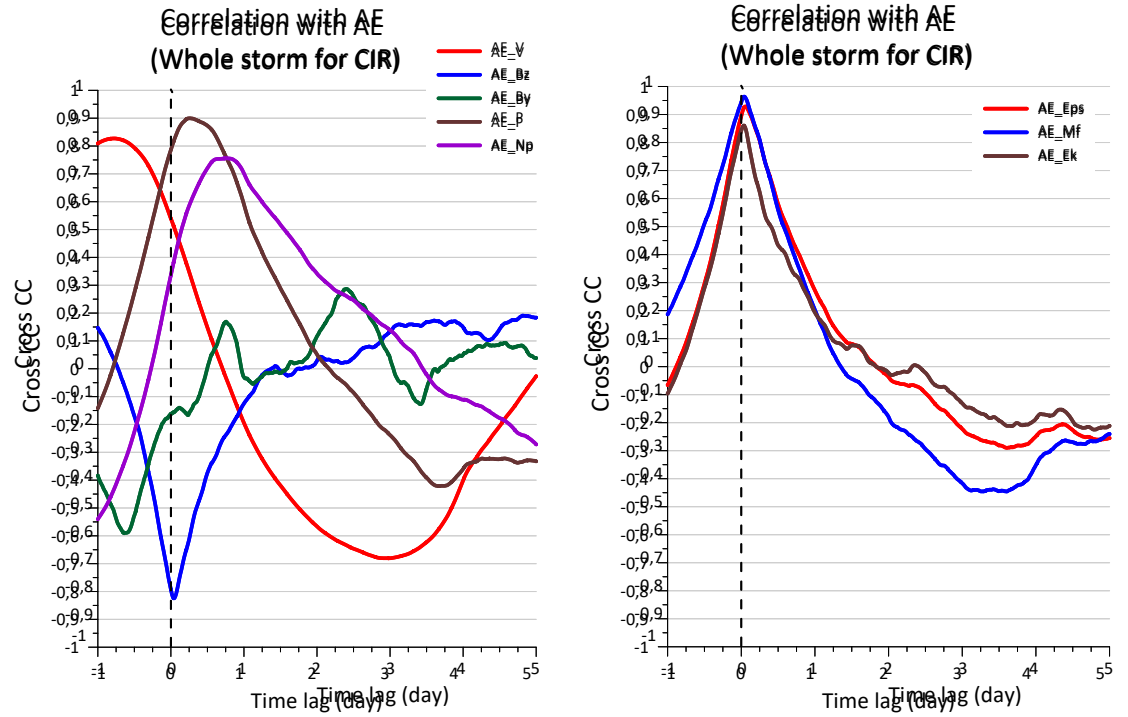

Figure 4. Variation of cross-correlation coefficients between *AE* and SW parameters including the solar wind velocity V_{SW}, dynamic pressure P_{SW}, proton density N_p, the interplanetary magnetic field B_y, B_z components respectively (left), and energy coupling functions (right) for a CIR-driven storm

The IMF B_y component changes direction, shifting from positive to negative values during the main and early recovery phases. This behavior is clearly reflected in the cross-correlation results, showing a peak $\Delta t \sim -15^h00^m$ with CC = –0.59. Numerous studies indicate that with the presence of the eastward-westward B_y component, the configuration of the magnetosphere changes, and the reconnection site in the dayside magnetosphere shifts [Tenfjord et al., 2015; Gong et al., 2022]. The direction of the IMF B_y component can influence the

rotation direction of the auroral oval in the Northern Hemisphere: clockwise during sunset orientation of IMF B_y and counterclockwise during its sunrise orientation, distorting the symmetric two-cell convection (banana-shaped and orange-peel-shaped) [Kullen, Blomberg, 1996; Liu et al., 2020]. In the ionosphere, the banana-shaped cell is observed in the dawn sector; and the orange-peel-shaped one, in the dusk sector for positive B_y [Tenfjord et al., 2015; Liu et al., 2020]. The IMF B_y component induces the B_y component in the magnetotail [Tenfjord et al., 2015; Gong et al., 2022; Case et al., 2018], thus the negative time lag indicates an indirect connection between them.

Regarding the activation of the ring current and its connection to energy coupling functions during CIR, shown in Figure 4 (left), these functions exhibit a negative correlation. This suggests that during energy dissipation the intensification of the ring current leads to a decrease in the global geomagnetic field, which is also confirmed by the epoch superposition results of geomagnetic storms. The highest correlation coefficient is observed for the magnetic flux rate $d\phi/dt$, with CC = −0.92 at $\Delta t \approx 5^{d}35^{m}$. The electric field energy at the magnetopause (E_{KL}) reaches its peak at approximately $\Delta t \approx 03^{h}$ with CC = −0.74. The *SYM-H* responds to the ponderomotive force function (electromagnetic energy — ε) at $\Delta t \approx 6^{h}$, where CC = −0.83.

In the case of the relationship between *AE* and the examined energy coupling functions, all parameters show a positive correlation with the auroral electrojet index, indicating their synchronous behavior. Among these parameters, the function $d\varphi/dt$ demonstrates the strongest correlation, with a maximum correlation coefficient (CC) of 0.96 at $\Delta t \sim 1$ hr. Meanwhile, the E_{KL} function reaches its peak at $\Delta t \sim 50$ min with CC = 0.86 (Figure 4, left). The epsilon function also exhibits a significant peak at $\Delta t \sim 1$ hr 20 min with CC = 0.93.

Overall cross-correlation results for CME/CIR events are summarized in Table. While the results also indicate the strongest correlations between geomagnetic indices and V_{SW} and N_p during CIR events, the highest peaks occurred at negative time lags. Similar findings were reported by Maggiolo et al. [2017], where V_{SW} lagged *SYM-H* by 26 hrs and *AE* by ~9 hrs, indicating an indirect relationship between the solar wind and the magnetic indices [Maggiolo et al., 2017]. The magnetospheric ring current response to the IMF B_z component is delayed for ~5 hrs for events of both types. This time lag reflects the time required for the convective electric field to penetrate and for disturbances to propagate from the shock front to the inner magnetosphere. IMF B_z is more strongly correlated with CIR-driven storms (CC = 0.71) compared to CME-driven events (CC = 0.62). The key parameter responsible for the opening of geomagnetic field lines on the dayside is the IMF B_z component. This suggests that, following significant IMF *Bz* activation at the L1 point, the evolution of the ring current is driven by particles from the plasma sheet, leading to a reduction in the global magnetic field, a process that takes ~5 hrs. This result is in contrast with those of other studies which have found that the growth phase of geomagnetic activity (*SYM-H*) occurs typically 1–2 hrs after IMF B_z turns southward (from northward) [Yermolaev et al., 2010].

The *AE* response time to the IMF B_z component is delayed for ~30–50 min for both CIR and CME events, which aligns with the findings of Stumpo et al. [1982**?**], who reported response times of *SYM-H* and *AE* indices to solar wind variations to be ~30–60 min. These findings are consistent with other analyses indicating that *AE* lags IMF B_z by roughly 20–30 min [Maggiolo et al., 2017; Polozov, 2020; Tsurutani et al., 1990; De Souza et al., 2018; Meng et al., 1973]. A ~30 min delay corresponds to the behavior of auroral electrojets, which is affected by the particle injection process as well as the time required for the disturbance to propagate from the shock front to the ionosphere [Stumpo et al., 2020].

For CME

		V_{SW}	P_{SW}	N_p	B_z	B_y	E_{SW}	$d\varphi/dt$	ε
SYM-H CME	CC	–0.86	–0.86	–0.71	0.62	–0.34	–0.75	–0.81	–0.83
	Lag	$3^{h}36^{m}$	$8^{h}30^{m}$	$15^{h}50^{m}$	$6^{h}50^{m}$	$2^{h}10^{m}$	$4^{h}48^{m}$	$5^{h}50^{m}$	$5^{h}18^{m}$
AE CME	CC	–0.69	0.95	0.85	–0.81	0.50	0.88	0.94	0.94
	Lag	$-5^{h}25^{m}$	$3^{h}00^{m}$	$5^{h}17^{m}$	$0^{h}33^{m}$	$5^{h}00^{m}$	$0^{h}15^{m}$	$0^{h}27^{m}$	$0^{h}15^{m}$

For CIR

		V_{SW}	P_{SW}	N_p	B_z	B_y	E_{SW}	$d\varphi/dt$	ε
SYM-H CIR	CC	–0.86	–0.85	–0.67	0.71	0.55	–0.74	–0.92	–0.83
	Lag	$8^{h}00^{m}$	$15^{h}30^{m}$	$1^{d}00^{h}45^{m}$	$4^{h}30^{m}$	$11^{h}55^{m}$	$3^{h}00^{m}$	$5^{h}35^{m}$	$6^{h}00^{m}$
AE CIR	CC	–0.83	0.90	0.76	–0.82	0.50	0.86	0.96	0.93
	Lag	$-18^{h}35^{m}$	$6^{h}20^{m}$	$18^{h}08^{m}$	$1^{h}00^{m}$	$5^{h}00^{m}$	$0^{h}50^{m}$	$1^{h}00^{m}$	$1^{h}20^{m}$

CONCLUSION

We have statistically analyzed 131 CME-driven and 161 CIR-driven storms that occurred during solar cycles 23 and 24. The main findings of the analysis are as follows:

1. For storms of both types, the development of the ring current is strongly influenced by solar wind parameters. The correlation coefficients are high, approximately –0.85, with the solar wind velocity V_{SW} and dynamic pressure P_{SW}. The correlation with the proton density N_p is slightly lower, with coefficients around –0.70. The interplanetary magnetic field parameters show weaker correlations compared to the solar wind parameters. However, energetic parameters demonstrate quite strong correlations, especially the rate of change in the magnetic flux $d\phi/dt$, which reaches values greater than –0.92 during CIR-driven storms.

2. During CME-driven storms, auroral activity strongly depends on SW and IMF parameters, except for V_{SW} (CC=–0.69). The IMF B_y component shows a higher correlation compared to *SYM-H*. Energetic parameters correlate strongly in the terms of both auroral activity and ring current development.

3. Time delays (Δt) in auroral activation relative to energetic parameters and IMF B_z are very short for CME-driven storms — about half an hour or less. For CIR-driven storms, the delay is around one hour. As for the ring current, for CME-driven storms the key parameters are V_{SW} and B_z; for CIR-driven storms, B_z is dominant. In both cases, energetic parameters exhibit development times ranging from 3 to 6 hrs on average, whereas the solar wind parameters, such as P_{SW} and N_p, have delays from 12 hrs to a full day. For auroral activity, the average delay is also 3 to 6 hrs, except for V_{SW} and N_p during CIR-driven storms.

REFERENCES

Akasofu S.I. Energy coupling between the solar wind and the magnetosphere. *Space Sci. Rev*. 1981, vol. 28, pp. 121–190. https://doi.org/10.1007/BF00218810.

Arnoldy R.L. Signature in the interplanetary medium for substorms. *J. Geophys. Res*. 1971, vol. 76, iss. 22, pp. 5189–5201. DOI: https://doi.org/10.1029/JA076i022p05189.

Baumjohann W., Treumann R.A. *Basic space plasma physics (revised edition)*. 2012, pp. 1–479. https://doi.org/10.1142/P850.

Borovsky J.E., Denton M.H. Differences between CME-driven storms and CIR-driven storms. *J. Geophys. Res*. 2006, vol. 111, iss. A7. https://doi.org/10.1029/2005ja011447.

Burton R.K., McPherron R.L., Russell C.T. An empirical relationship between interplanetary conditions *and Dst*. *J. Geophys. Res*. 1975, vol. 80, iss. 31, pp. 4204–4214. https://doi.org/10.1029/ja080i031p04204.

Case N.A., Grocott A., Haaland S., et al. Response of Earth's Neutral Sheet to Reversals in the IMF B_y Component. *J. Geophys. Res.: Space Phys*. 2018, vol. 123, iss. 10, pp. 8206–8218. https://doi.org/10.1029/2018JA025712.

Chen M.W. Chapter 5 — Ring current development. *Ring Current Investigations. Edited V.K. Jordanova, R. Ilie and M.W. Chen*. 2020, Elsevier: 153–180. https://doi.org/10.1016/B978-0-12-815571-4.00005-6.

Davis T.N., Sugiura M. Auroral Electrojet Activity Index *AE* and its universal time variations. *J. Geophys. Res*. 1966, vol. 71, iss. 3, pp. 785–801.

De Souza A.M., Echer E., M. Bolzan J.A., Hajra R. Cross-correlation and cross-wavelet analyses of the solar wind IMF B_z and auroral electrojet index *AE* coupling during HILDCAAs. *Ann. Geophys*. 2018, vol. 36, iss. 1, pp. 205–211. https://doi.org/10.5194/angeo-36-205-2018.

Dungey J.W. Interplanetary magnetic field and the auroral zones. *Phys. Rev. Lett*. 1961, vol. 6, iss. 2, pp. 47–48. https://doi.org/10.1103/PhysRevLett.6.47.

Fuselier S.A., Petrinec S.M., Trattner K.J. Stability of the high-latitude reconnection site for steady northward IMF. *Geophys. Res. Lett*. 2000, vol. 27, iss. 4, pp. 473–476. https://doi.org/10.1029/1999GL003706.

Gong F., Yu Y., Cao J. Simulating the Responses of the Magnetosphere–Ionosphere System to the IMF B_y Reversal. *Front. Phys*. 2022, vol. 10, pp. 1–8. https://doi.org/10.3389/fphy.2022.900192.

Gonzalez W.D., Joselyn J.A., Kamide Y., et al. What is a geomagnetic storm? *J. Geophys. Res*. 1994, vol. 99, iss. A4. https://doi.org/10.1029/93ja02867.

Gunell H., Nilsson H., Stenberg G., et al. Plasma penetration of the dayside magnetopause. *Phys. Plasmas*. 2012, vol. 19, 072906. https://doi.org/10.1063/1.4739446.

Hasegawa H., Fujimoto M., Phan T.D., et al. Transport of solar wind into Earth's magnetosphere through rolled-up Kelvin–Helmholtz vortices. *Nature*. 2004, vol. 430, pp. 755–758. https://doi.org/10.1038/nature02799.

Hutchinson J.A., Wright D.M., Milan S.E. Geomagnetic storms over the last solar cycle: A superposed epoch analysis. *J. Geophys. Res. Sp. Phys*. 2011, vol. 116, iss. 9, pp. 1–16. https://doi.org/10.1029/2011JA016463.

Kamide Y., Baumjohann W., Daglis I., et al. Current understanding of magnetic storms: Storm-substorm relationships. *J. Geophys. Res.: Space Phys*. 1998, vol. 103, iss. A8, pp. 17705–17728. https://doi.org/10.1029/98ja01426.

Kan J.R., Lee L. C. Energy coupling function and solar wind-magnetosphere dynamo. *Geophys. Res. Lett*. 1979, vol. 6, iss. 7, pp. 577–580. https://doi.org/10.1029/GL006i007p00577.

Kan J.R., Lee L.C., Akasofu S.I. The energy coupling function and the power generated by the solar wind-magnetosphere dynamo. *Planet. Space Sci*. 1980, vol. 28, iss. 8, pp. 823–825. https://doi.org/10.1016/0032-0633(80)90080-X.

Kremser G., Lundin R. Average spatial distributions of energetic particles in the midaltitude cusp/cleft region observed by Viking, *J. Geophys. Res*. 1990, vol. 95, iss. A5, pp. 5753–5766. https://doi.org/10.1029/JA095iA05p05753.

Kullen A., Blomberg L.G. The influence of IMF B_y on the mapping between the Earth's magnetotail and its ionosphere. *Geophys. Res. Lett*. 1996, vol. 23, iss. 18, pp. 2561–2564. https://doi.org/10.1029/96GL02305.

Lethy A., El-Eraki M. A., Samy A., Deebes H. A. Prediction of the *Dst* Index and Analysis of Its Dependence on Solar Wind Parameters Using Neural Network Sp. Weather. 2018, vol. 16, iss. 9, pp. 1277–1290. DOI: https://doi.org/10.1029/2018SW001863.

Liang J., Donovan E., Nishimura Y., et al. Low-energy ion precipitation structures associated with pulsating auroral patches. *J. Geophys. Res.: Space Phys*. 2015, vol. 120, pp. 5408–5431. https://doi.org/10.1002/2015JA021094.

Liu J., Burns A. G., Wang W., Zhang Y. Modeled IMF B_y Effects on the Polar Ionosphere and Thermosphere Coupling. *J. Geophys. Res.: Space Phys*. 2020, vol. 125, iss. 3, pp. 1–15. https://doi.org/10.1029/2019JA026949.

Maggiolo R., Hamrin M., De Keyser J., et al. The Delayed Time Response of Geomagnetic Activity to the Solar Wind. *J. Geophys. Res.: Space Phys*. 2017, vol. 122, iss. 11. https://doi.org/10.1002/2016ja023793.

Meng C.-I., Tsurutani B., Kawasaki K., Akasofu S.-I. Cross-correlation analysis of the *AE*-index and the interplanetary magnetic field B_z component. *J. Geophys. Res*. 1973, vol. 78, iss. 4, pp. 617–629. https://doi.org/10.1029/ja078i004p00617.

Namuun B., Tsegmed B., Li L. Y., Leghari G.M. Differences in the response to CME and CIR drivers of geomagnetic disturbances. *Sol.-Terr. Phys*. 2023, vol. 9, iss. 2, pp. 31–36. 10.12737/stp-92202304.

Newell P.T., Sotirelis T., Liou K., Meng C.I., Rich F.J. A nearly universal solar wind-magnetosphere coupling function inferred from 10 magnetospheric state variables. *J. Geophys. Res.: Space Phys*. 2007, vol. 112, iss. 1, p. A01206. https://doi.org/10.1029/2006ja012015.

Ondoh T. Correlation of *AE* activity with IMF-B_z during small geomagnetic storms. *Adv. in Space Res.* 2000, vol. 26, iss. 1, pp. 111–116. https://doi.org/10.1016/S0273-1177(99)01035-2.

Paschmann G., Sonnerup B., Papamastorakis I., et al. Plasma acceleration at the Earth's magnetopause: evidence for reconnection. *Nature*. 1979, vol. 282, pp. 243–246. https://doi.org/10.1038/282243a0.

Perreault P., Akasofu S.-I. A study of geomagnetic storms. *Geophys. J. Royal Astron. Soc*. 1978, vol. 54, iss. 3, pp. 547–573. https://doi.org/10.1111/j.1365-246X.1978.tb05494.x.

Polozov Y. Analysis of the data of IMF B_z and *AE*-index for the period 1999–2018. *E3S Web of Conferences*. 2020, vol. 196. https://doi.org/10.1051/e3sconf/202019602005.

Potapov A.S. ULF wave activity in high-speed streams of the solar wind: Impact on the magnetosphere, *J. Geophys. Res.: Space Phys*. 2013, vol. 118, pp. 6465–6477. https://doi.org/10.1002/2013JA019119.

Richardson I.G., Cane H.V. Particle flows observed in ejecta during solar event onsets and their implication for the magnetic field topology. *J. Geophys. Res.: Space Phys*. 1996, vol. 101, iss. A12, pp. 27521–27532. https://doi.org/10.1029/96ja02643.

Rostoker G., Fälthammar C.-G. Relationship between changes in the interplanetary magnetic field and variations in the magnetic field at the Earth's surface. *J. Geophys. Res*. 1967, vol. 72, iss. 23, pp. 5853–5863. https://doi.org/10.1029/jz072i023p05853.

Rout D., Patra S., Kumar S., et al. The Growth of Ring Current/*SYM-H* Under Northward IMF B_z Conditions Present During the 21–22 January 2005 Geomagnetic Storm. *Space Weather*. 2023, vol. 21, iss. 10, pp. 1–11. https://doi.org/10.1029/2023SW003489.

Stepanov N.A., Sergeev V., Sormakov D., et al. Superthermal Proton and Electron Fluxes in the Plasma Sheet Transition Region and Their Dependence on Solar Wind Parameters. *J. Geophys. Res.: Space Phys*. 2021, vol. 126, iss. 4. DOI: https://doi.org/10.1029/2020ja028580.

Stumpo M., Consolini G., Alberti T., Quattrociocchi V. Measuring information coupling between the solar wind and the magnetosphere-ionosphere system. *Entropy*. 2020, vol. 22, iss. 3, pp. 1–14. https://doi.org/10.3390/e22030276.

Sugiura M. Hourly values of equatorial *Dst* for the IGY. *Ann. Int. Geophys. Year*. 1963, vol. 35, pp. 9–45.

Tenfjord P., Østgaard N., Snekvik K., et al. How the IMF B_y induces a B_y component in the closed magnetosphere and how it leads to asymmetric currents and convection patterns in the two hemispheres. *Annals of the International Geophysical Year*. 2015, vol. 120, iss. 11, pp. 9368–9384. https://doi.org/10.1002/2015JA021579.

Troshichev O.A., Sormakov D.A. PC index as a proxy of the solar wind energy that entered into the magnetosphere: 4. Relationship between the solar wind dynamic pressure (PSW) impulses and PC, AL indices. *J. Atmos. Solar-Terr. Phys*. 2019, vol. 182, pp. 200–210. https://doi.org/10.1016/j.jastp.2018.12.001.

Tsurutani B.T., Thorne R.M. Diffusion processes in the magnetopause boundary layer. *Geophys. Res. Lett.* 1982. https://doi.org/10.1029/GL009i011p01247.

Tsurutani B.T., Gonzalez W.D., Tang F., Akasofu S.I., Anderson R.R. The interplanetary and solar causes of geomagnetic activity. *Planet. Space Sci.* 1990, vol. 38, iss. 1, pp. 109–126. https://doi.org/10.1016/0032-0633(90)90010-N.

Tsurutani B.T., Gonzalez W.D., Clúa de Gonzalez A.L., et al. Corotating solar wind streams and recurrent geomagnetic activity: A review. *J. Geophys. Res.: Space Phys*. 2006, vol. 111, iss. 7, pp. 1–25. https://doi.org/10.1029/2005JA011273.

Tsyganenko N.A., Mukai T. Tail plasma sheet models derived from Geotail particle data. *J. Geophys. Res.: Space Phys*. 2003, vol. 108, iss. A3, pp. 1–15. https://doi.org/10.1029/2002JA009707.

Yamada M., Kulsrud R., Ji H. Magnetic reconnection. *Reviews of Modern Physics*. 2010, vol. 82 (1), pp. 603–664. https://doi.org/10.1103/revmodphys.82.603.

Yermolaev Y.I., Nikolaeva N.S., Lodkina I.G., Yermolaev M.Y. Specific interplanetary conditions for CIR-, Sheath-, and ICME-induced geomagnetic storms obtained by double superposed epoch analysis. *Ann. Geophys*. 2010, vol. 28, pp. 2177–2186. https://doi.org/10.5194/angeo-28-2177-2010.

URL: https://omniweb.gsfc.nasa.gov (accessed March 31, 2025).

Original Russian version: Tsegmed B., Namuun B., published in Solnechno-zemnaya fizika. 2026, vol. 12, no. 2, pp. 38–46. https://doi.org/10.12737/szf-122202604.

How to cite this article

Tsegmed B., Namuun B. Statistical study of predictive parameters for geomagnetic storms during solar cycles 23–24. *Sol.-Terr. Phys*. 2026, vol. 12, iss. 2, pp. 34–42. https://doi.org/10.12737/stp-122202604.